Analysis of radiation belt energetic electron phase space density using THEMIS SST measurements: Cross-satellite calibration and a case study

Binbin Ni,[1] Yuri Shprits,[1,2] Michael Hartinger,[2,3] Vassilis Angelopoulos,[2,3] Xudong Gu,[4] and Davin Larson[5]

Received 8 September 2010; revised 29 November 2010; accepted 3 January 2011; published 10 March 2011.

[1] In this study we perform an energy channel dependent cross-satellite calibration of Time History of Events and Macroscale Interactions during Substorms (THEMIS) solid state telescope (SST) flux measurements based on electron phase space density (PSD) conjunctions at fixed phase space coordinates. By comparing PSD around L* = 6 between THEMIS SST and Los Alamos National Laboratory (LANL) satellite LANL-01A synchronous orbit particle analyzer (SOPA) for a half year period starting from 1 July 2007, we evaluate systematic errors in the THEMIS SST measurements and quantify the cross-instrument calibration factors for the 11 SST energy channels from 40 to 2159 keV. Good consistency in electron PSD conjunctions between the five THEMIS probes indicates that the SST instrument aboard each spacecraft responds quite similarly to the ambient electron radiation environment. Compared to the LANL-01A SOPA instrument, the THEMIS SST underestimates the electron fluxes within a factor of 2 for the 40–140 keV energy channels and overestimates the electron fluxes within a factor of 3 for the 204–2159 keV energy channels. Using the cross-satellite calibrated SST flux data for the five THEMIS spacecraft and the SOPA measurements from the LANL-01A and 1989–048 satellites, we analyze the response of radiation belt electrons to a sudden solar wind pressure enhancement event. The electron PSD conjunctions between the THEMIS probes and the two geostationary satellites show good agreement, suggesting a reasonable cross-satellite calibration of the SST measurements. Our results also indicate a clear correlation between electron PSD dropouts and the solar wind pressure pulse, which is likely due to the combination of magnetopause shadowing and outward radial diffusion. The gradual buildup of electron PSD after the abrupt pressure enhancement most likely results from a combined effect of local acceleration and inward and outward radial diffusion that refills the main phase PSD dropout when the magnetopause moves outward. A longer-term quantitative analysis of the temporal evolution and radial profile of electron PSD based on multiple satellite measurements, including the cross-satellite calibrated THEMIS SST data, will be required to improve our understanding of the dynamic responses of radiation belt electrons to solar activity.

Citation: Ni, B., Y. Shprits, M. Hartinger, V. Angelopoulos, X. Gu, and D. Larson (2011), Analysis of radiation belt energetic electron phase space density using THEMIS SST measurements: Cross-satellite calibration and a case study, *J. Geophys. Res.*, *116*, A03208, doi:10.1029/2010JA016104.

1. Introduction

[2] The Time History of Events and Macroscale Interactions during Substorms (THEMIS) mission [*Sibeck and Angelopoulos*, 2008] employs five identical satellites (a, b, c, d, and e) to track the motion of magnetospheric particles, plasma and waves in near-equatorial orbits with apogees above 10 Earth radii (R_E) and perigees below 2 R_E. While the primary goal of THEMIS is to elucidate the magnetotail process responsible for substorm onset, radiation belt science objectives are additionally addressed by the frequent probe traversals of the Earth's radiation belts. A number

[1]Department of Atmospheric and Oceanic Sciences, University of California, Los Angeles, California, USA.
[2]Institute of Geophysics and Planetary Physics, University of California, Los Angeles, California, USA.
[3]Department of Earth and Space Sciences, University of California, Los Angeles, California, USA.
[4]Department of Space Physics, Wuhan University, Wuhan, Hubei, China.
[5]Space Sciences Laboratory, University of California, Berkeley, California, USA.

0148-0227/11/2010JA016104

of studies have been performed on the basis of THEMIS observations to improve our understanding of radiation belt physics. Using the THEMIS measurements, including the electrostatic analyzer (ESA) [*McFadden et al.*, 2008] electron phase space density data, the filter bank mode wave data [*Cully et al.*, 2008] analyzed from the outputs of Electric Field Instrument (EFI) [*Bonnell et al.*, 2008] and Search Coil Magnetometer (SCM) [*Roux et al.*, 2008; *Le Contel et al.*, 2008], the Fluxgate Magnetometer (FGM) [*Auster et al.*, 2008] magnetic field data and spacecraft potential data, *Li et al.* [2009a, 2009b, 2010] have performed detailed investigations of the global distribution of whistler mode chorus emissions and their optimum excitation conditions. These emissions play important roles in both acceleration and loss processes for energetic radiation belt electrons and the plasma sheet electron source population [e.g., *Horne et al.*, 2005; *Thorne et al.*, 2005; *Summers et al.*, 2007; *Ni et al.*, 2008; *Shprits et al.*, 2008a, 2008b].

[3] Since the energetic radiation belt electron fluxes are highly dynamic, in particular during geomagnetic storms [e.g., *Reeves et al.*, 2003], reliable spaceborne observations of electron flux in time and space are a key ingredient to understand the underlying physical processes of electron transport, acceleration, and loss. While originally designed to measure the upper end of particle distributions for the determination of complete moments and to identify current boundaries, the THEMIS solid state telescope (SST) instrument can also provide measurements of the radial profile of energetic electron fluxes from ~30 keV to ~900 MeV on rapid timescales [*Angelopoulos*, 2008; *Angelopoulos et al.*, 2008; D. Larson, Using the THEMIS energetic particle data, http://www.virbo.org/Image:THEMIS-SST.ppt, 2009]. Each SST detector system consists of two identical detector heads (data available at http://www.virbo.org/Image:THEMIS-SST.ppt). Each head has two sides, each measuring electrons and ions over a field of view of 37° and mounted on the spacecraft skin at a view angle of 52° and 25° relative to the spin plane, thereby covering nearly the full sphere during a spacecraft spin [see *Angelopoulos*, 2008, Figure 8]. In the electron direction protons < 350 keV are stopped by a thin foil (F) ahead of the "F" detector while in the ion side ions have an open (O) path to the detector and <350 keV electrons are deflected by a magnet. A detector between the "O" and the "F" detectors is twice as thick (T) as the others and records > 350 keV electrons that have enough energy to penetrate through the "F" side or can make themselves through the "O" magnet and the "O" detector, but not ions unless their energies are larger than 6 MeV. Coincidence logic detects "FT" and "OT" events separately and bins them into separate energy channels. "F" counts below 350 keV are reasonable estimates of the electron fluxes below 350 keV. Between 350 keV and 2 MeV, most electrons are deposited in the "T" detector and are thus best sensed by the "FT" channels. Since a significant number of 0.35–2 MeV electrons also scatter inside the "F" detector before their subsequent passage into the "T" detector, a portion of the "F" counts in the lower half of this energy range are also due to energetic electrons. However, since >350 keV protons cannot be completely stopped by the thin foil, they may have enough energy to both penetrate the "F" detector foil and deposit sufficient energy (>25 keV) to be recorded into the "F" detector energy channels. At an energy range of a few hundred keV, where ~300 keV electron fluxes dominate above ~650 keV proton fluxes, the proton contamination effect is expected to be negligible. At higher energies > 350 keV, where the "F" detector response to electrons diminishes thanks to the fact that electrons cannot be fully stopped by the "F" detector, the proton contamination starts to become more dominant. However, because of the preponderance of 0.5–1 MeV electron fluxes relative to lower-energy (by 350 keV) proton fluxes and the scattering of energetic electrons in the detector itself and the walls prior to their entry into the detector, even higher-energy channels respond to the ambient electron fluxes.

[4] With a broad energy coverage from the radiation belt electron source population to hazardous relativistic electrons as well as available pitch angle information for each energy channel, the SST data from the five-probe THEMIS mission has enormous potential for studying radiation belt electron dynamics. However, in addition to the limited shielding and partly because of the two-ended telescope design of the instrument that results in the aforementioned spurious effects beyond 350 keV, sunlight contamination of the open ion detector ("O") affects all channels (including "F" channels) because of electronic cross talk. Note that while operation of an attenuator with x60 flux reduction at times of high activity makes actual instrument saturation rare, occasionally dead-time correction is required if count rates are a good fraction of saturation levels (>20 kHz/channel). Finally, the lowest-energy channel electrons are subject to foil scattering (defocusing) and resultant reduction in low-energy electron flux. Although this can now be routinely calibrated away, the data used in this study have not incorporated this correction; and the resultant scaling derived in this study encompasses the foil scattering effect (data available at http://www.virbo.org/Image:THEMIS-SST.ppt).

[5] A number of standard techniques are available for removal of some of the above SST spurious effects. Sunlight contamination, which affects all the energy channels, can be removed when the full particle distribution is used by subtracting a constant electronic noise background on a case-by-case basis. Additional calibration methods have already been employed to reduce some of the uncertainties associated with the SST electron fluxes. This involves searching for steady periods of moderately high flux with a single population with a simple energy spectrum, usually monotonically decreasing at high energies, and determining the geometric factor for electrons based on a comparison with the ESA electron spectrum and an extrapolation to higher energies. Additionally, ground calibration involves creating a partial 3D model of the instrument and simulating its response and background noise to an ambient electron spectrum using the GEANT4 software [*Agostinelli et al.*, 2003]. The latter effort, which can help determine the SST instrument response to both scattered and penetrating electrons, is currently under way. While the above calibration efforts have continued to improve the absolute accuracy of the SST electron flux, important information can be obtained, especially for operational use in models, when comparing the THEMIS SST measurements to the Synchronous Orbit Particle Analyzer (SOPA) observations onboard

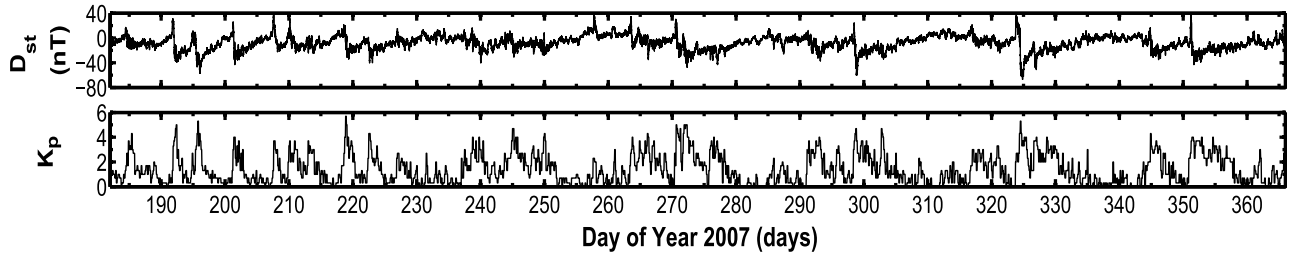

Figure 1. The time series of geomagnetic indices (top) Dst and (bottom) Kp for a half year period from 1 July to 31 December 2007.

the LANL (Los Alamos National Laboratory) satellites. Cross-satellite calibration can be also referred to as empirical since it is basically based on observations as opposed to theoretical or modeling estimates.

[6] Such empirical cross-satellite calibration efforts can then be used as an independent validation of the THEMIS SST efficiencies derived from instrument simulations and can also immediately extend the coverage of geosynchronous assets in radial distance or local time, for a more complete study of the radiation belt and its variability. As long as there is at least one reference satellite with well-calibrated energy response, simultaneous measurements from multiple satellites provide a good opportunity to perform such cross-satellite calibration. For example, using the CRRES (Combined Release and Radiation Effects Satellite), LANL GEO, and Polar electron data that covers a period of three full solar cycles from 1976 to 2005, *Friedel et al.* [2005] conducted a statistical intercalibration of magnetospheric energetic electron data. By establishing a common geomagnetic coordinate system for all the satellites with the static OP77 magnetic field model [*Olson and Pfitzer*, 1977], they obtained a statistically meaningful set of conjunctions of electron flux data for the evaluation of feasible adjustment factors between any two instruments. Intersatellite calibrations can also be implemented on using electron phase space density (PSD) conjunctions at the same set of phase space coordinates (PSCs) or equally the three adiabatic invariants (μ, K, L^*), because Liouville's theorem requires that electron PSD be conserved at the same PSCs (but at different phases along the particle drift trajectory) in the absence of any loss or source. This method significantly increases the number of conjunctions and permits comparisons between measurements in different MLT sectors. *Chen et al.* [2005] called this method "fine-tuned" calibration and implemented it between three LANL GEO satellites for a geomagnetically quiet period. *Ni et al.* [2009a, 2009b] adopted a similar approach and performed cross-instrument calibrations between the satellite pairs of CRRES/Akebono and CRRES/LANL GEO.

[7] In this study we perform cross-satellite calibration of THEMIS SST data based on electron PSD conjunctions with high-quality LANL SOPA measurements. Through a robust, although strict selection of PSD conjunctions corresponding to each THEMIS SST energy channel of interest, energy channel dependent cross-satellite calibrations will be examined carefully. In section 2 we give a brief description of the data set to be analyzed and the methodology of electron PSD calculation and intersatellite calibration. Section 3 presents the evaluations of cross-satellite calibration factors for each THEMIS spacecraft using a half year of SST flux data and FGM magnetic field measurements, together with an initial study of radiation belt electron PSD radial profiles using LANL SOPA and cross-satellite calibrated THEMIS SST measurements. We finally discuss our results in section 4 and make concluding remarks in section 5.

2. Data Availability and Methodology for Phase Space Density Calculation

[8] We focus on a half year period from 1 July 2007 to 31 December 2007. The corresponding time series of the geomagnetic indices Kp and Dst is shown in Figure 1. During the majority of the time span, Kp < 4 and Dst > −40 nT, indicative of relatively low-geomagnetic activity, which ensures that adiabatic invariants are not substantially violated during a particle's drift time and that global magnetic field models are sufficiently accurate.

[9] Energetic radiation belt electron flux data are collected simultaneously from the THEMIS SST and LANL SOPA instruments. The THEMIS spacecraft, comprising 5 probes in the near-equatorial orbits with apogees above 10 Re and perigees below 2 Re, are ideally situated to measure electron fluxes in the equatorial magnetosphere. We convert counts from the SST instrument to electron energy flux using software released by the THEMIS mission (released 12 November 2009). To do this, we make use of the following relationship

$$EnergyFlux(E,\theta) = Counts(E,\theta) * \frac{E}{dT * \sigma * \alpha * dE}, \quad (1)$$

where E is the representative energy for the channel with $E = (E1 + E2)/2$, dE is the width of the energy channel with $dE = E2 - E1$, $E1$ and $E2$ are the low- and high-energy bounds for the channel, θ is the pitch angle, dT is the accumulation time (0.1875 s), σ is the geometric factor (0.1 cm^2/steradian), and α is the attenuator scaling factor (1 or 1/64, depending on attenuator status). As of the writing of this paper, there were no additional factors applied to the counts data in the software, although that may change in the future as, for example, low-energy data from the SST detector are compared to high-energy data from the electrostatic analyzer. The data have also been cleaned of sunlight

contamination and electronic noise, but have not yet been validated with other measurements. This database provides differential electron flux information for 16 energy channels covering an energy range from ~30 keV to >5 MeV with inherent pitch angle resolution of 22.5–37° but interpolated and binned in 5° pitch angle increments. The ambient magnetic field data are also obtained from the THEMIS FGM measurements to facilitate the determination of the first adiabatic invariant. The geostationary LANL SOPA [*Belian et al.*, 1992] in one spin measures the electron distribution from 50 keV to more than 1.5 MeV in 10 energy channels. In this study we use pitch angle averaged differential fluxes evaluated at 16 energies between 24 keV and 4 MeV based on a reasonable fit of electron fluxes by two relativistic Maxwellian functions for the SOPA electron channels. The LANL SOPA flux data has been well calibrated through careful cross-instrument calibration with the CRRES MEA observations [e.g., *Friedel et al.*, 2005] and thus can act as a reliable standard for reference. Since these satellites carry no magnetometer, we adopt a magnetic field model for computation of the first adiabatic invariant.

[10] Cross-satellite calibration involves two processes: (1) converting electron fluxes to electron PSD and (2) comparing PSD conjunctions in accordance to their (μ, K, L^*) and evaluating the energy-dependent systematic differences. Since there are two categories of differential electron flux, directional for THEMIS SST data and omnidirectional (or pitch angle averaged) for LANL SOPA data, two different methods have been used to infer electron PSD from the satellite observations. Readers are referred to *Ni et al.* [2009a, 2009b] for the detailed methodology of phase space density calculation using these two different types of flux information. A brief description is given below.

[11] For the THEMIS SST electron flux data as a function of electron energy, local pitch angle and satellite position, we start with a specific μ value and an array of local pitch angle α to calculate corresponding values of K and L^* using the ONERA-DESP library V4.2 (http://craterre.onecert.fr/support/user_guide.html). The corresponding energies E_k are also determined with local magnetic field information. Assuming an exponentially decaying energy spectrum, we interpolate between neighboring energy channels to obtain the differential fluxes for these energies, which are then transformed to phase space densities. Finally, for any K value of interest, we apply a linear interpolation between two adjacent K points to obtain both the electron PSD and the Roederer L^* value. For the LANL SOPA pitch angle averaged electron flux measurements, knowledge of pitch angle distribution is required to infer electron PSD. We assume that the radiation belt electron pitch angle distribution follows a power law function of the sine of pitch angle: $J(\alpha_{eq}) \propto \sin^n\alpha_{eq}$ [e.g., *Vampola*, 1998; *Gannon et al.*, 2007; *Selesnick and Kanekal*, 2009; *Gu et al.*, 2011]. Combination with the assumed exponential energy spectrum yields a pitch angle and energy-dependent electron differential flux model as $J(E_k, \alpha_{eq}) = Ae^{BE_k} \sin^n\alpha_{eq}$, where A, B are constants determined from the measurements and n is the power law index. Figure 2 shows the variations of the power index n with MLT sector and Kp at L = 6.0 and 6.6 based on a statistical analysis of CRRES MEA energy and pitch angle resolved flux data. The n value is apparently strongly dependent on the MLT region because of various loss and acceleration processes in different portions of the electron's drift orbit, while it is less sensitive to the Kp index especially for Kp ≤ 6. The CRRES MEA data also shows a slightly energy-dependent pitch angle distribution for energetic radiation belt electron [*Vampola*, 1998; *Gannon et al.*, 2007]. Based on the statistical results in Figure 2, we choose n = 0.1, 0.6, 1.0, 1.5, 0.4, and 0.0 for the MLT intervals of 00–04, 04–08, 08–12, 12–16, 16–20, and 20–24, respectively, which are subsequently incorporated into the PSD evaluations using the LANL SOPA pitch angle averaged electron flux measurements.

3. Analysis Results

[12] To apply reliable cross-instrument calibrations between the satellites that generally make measurements at different azimuthal locations, we need to concentrate on the trapped population of radiation belt electrons that suffer no losses as they drift around the Earth. In this study we choose a fixed value for the second adiabatic invariant, K = 0.05 $G^{0.5}$ R_E, corresponding to electrons with high α_{eq} of 61° at L = 6 in a dipole model. Owing to the geosynchronous orbits of the LANL satellites, we can expect that the majority of the PSD conjunctions occur around L^* = 6 for THEMIS and LANL satellites, and correspondingly there is an optimal value of the first adiabatic invariant μ, for each THEMIS SST energy channel, to perform careful energy-dependent calibration. Because of the possibly large uncertainties in the high-energy channels, here we analyze the SST flux data of the 11 energy channels from 40 keV to 2159 keV with the selected corresponding pairs of (μ, K) at L = 6 tabulated in Table 1. The dependences of equatorial pitch angle α_{eq} and electron energy E_k on L shell for these (μ, K) pairs are plotted in Figure 3 for a dipole magnetic field model. The energies at L = 6 are exactly equal to the representative energies for each THEMIS SST energy channel.

[13] Figure 4 presents an example of inferred electron PSD versus L^* distribution and the performance of cross-instrument calibration for a specific SST energy channel (66 keV). The value of μ is 37 MeV G^{-1} and K is 0.05$G^{0.5}$ R_E. Figures 4a and 4b show the original hourly averaged electron PSD computed using the Tsyganenko 96 (T96) model [*Tsyganenko and Stern*, 1996] and the measurements from THEMISd and LANL-01A, respectively. The PSD data inferred from the LANL SOPA measurements (Figure 4b) has good time resolution but is mostly limited to L^* from 5.5 to 6.2, consistent with the relatively low-geomagnetic activity during the considered time period. In contrast, analysis of the THEMISd SST data (Figure 4a) presents larger temporal gaps but a broader radial coverage of inferred electron PSD. To assure that we select the PSD conjunctions associated with the 66 keV energy channel under investigation, we confine the occurrences of PSD conjunctions to a narrow L^* range, 5.9 < L^* < 6.1, and infer PSD at μ = 37 MeV G^{-1} and K = 0.05$G^{0.5}$ R_E, which corresponds to an electron energy of 66 keV in a dipole model. The identified PSD conjunctions are shown in Figure 4c. With the dashed diagonal line of slope = 1 denoting perfect agreement between the

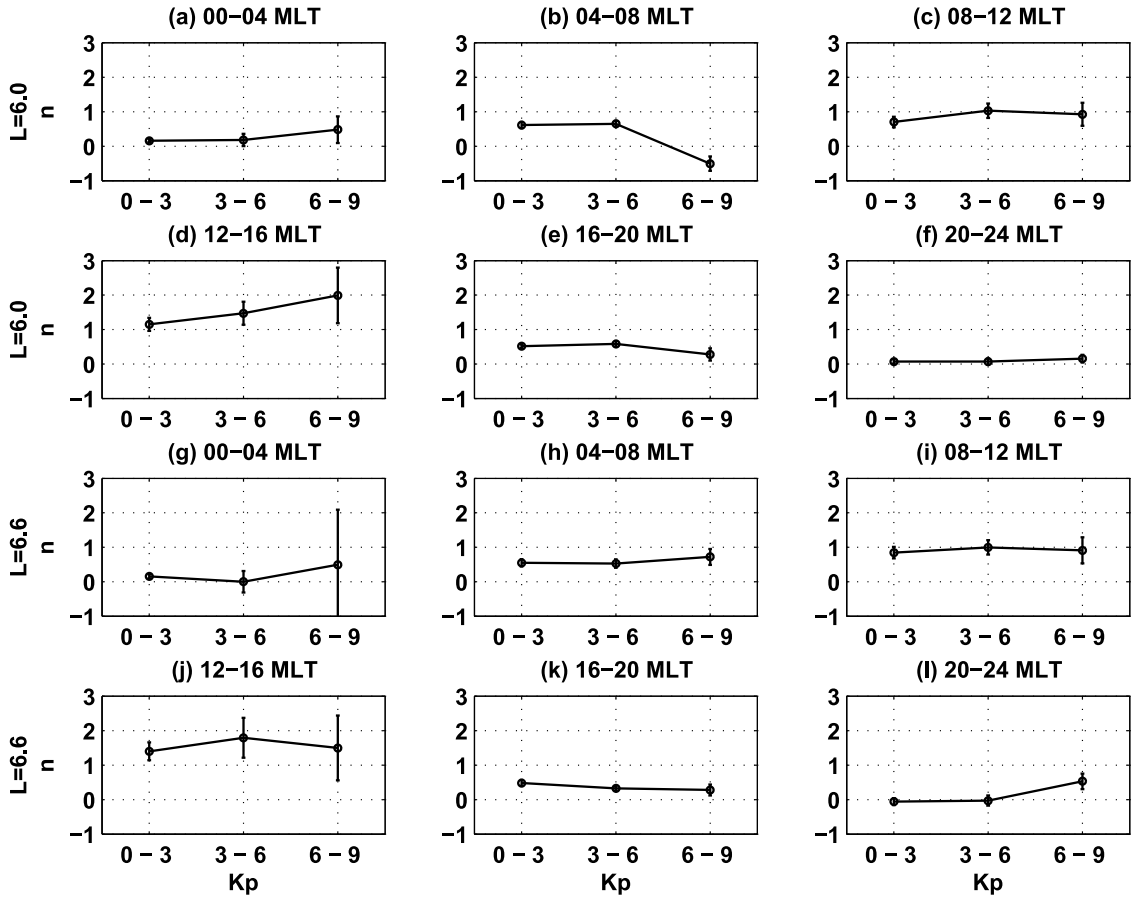

Figure 2. Averaged pitch angle distribution coefficient n as a function of Kp for six representative MLT sectors of 00–04, 04–08, 08–12, 12–16, 16–20, and 20–24 at the spatial location of (a–f) L = 6.0 ± 0.1 and (g–l) L = 6.6 ± 0.1, obtained through a statistical analysis of CRRES MEA electron flux measurements.

data, we can see most of the conjunction points located above it, indicating that the THEMIS SST data from this energy channel shows most often a lower PSD than the LANL SOPA measurements of particles with the same adiabatic invariants. To further investigate the systematic difference between these PSD conjunctions, we introduce the normalized difference (ND):

$$\text{Normalized difference} = \frac{PSD_2 - PSD_1}{(PSD_1 + PSD_2)/2} \times 100\%, \qquad (2)$$

where PSD_1 and PSD_2 are electron PSDs inferred from the THEMIS SST and LANL SOPA data, respectively. A histogram of the NDs is shown in Figure 4d, revealing a distribution peaked between −70% and −30%. This suggests that THEMISd SST fluxes at 66 keV systematically underestimate the PSD compared to the LANL SOPA data. Multiplying the THEMISd electron PSD by a constant of 1.62, we can minimize the averaged absolute difference and standard deviation of PSD conjunctions for this satellite pair. The scatter of PSD conjunctions and the histogram of the occurrences of PSD conjunctions over ND interval after the cross-satellite calibration are presented in Figures 4e and 4f, respectively. The distribution of the number of PSD conjunctions exhibits a Gaussian variation around ND = 0, indicating an excellent cross-instrument calibration for the THEMISd SST 66 keV energy channel with the LANL SOPA spectrum.

[14] Determination of electron PSD for fixed PSCs enables us to investigate the degree of consistency in electron flux measurements from the SST instruments individually onboard the five THEMIS probes. For each THEMIS

Table 1. Pairs of the First Two Adiabatic Invariants (μ, K) Whose Associated Electron Energies at L = 6 in a Dipolar Magnetic Field Correspond to the 11 Energy Channels of the THEMIS SST Instrument From 40 keV to 2159 keV

E_k (keV)	μ (MeV/G)	K ($G^{0.5}$ R_E)
40	22	0.05
52	29	0.05
66	37	0.05
93	54	0.05
140	84	0.05
204	130	0.05
292	200	0.05
415	311	0.05
634	548	0.05
1089	1198	0.05
2159	3581	0.05

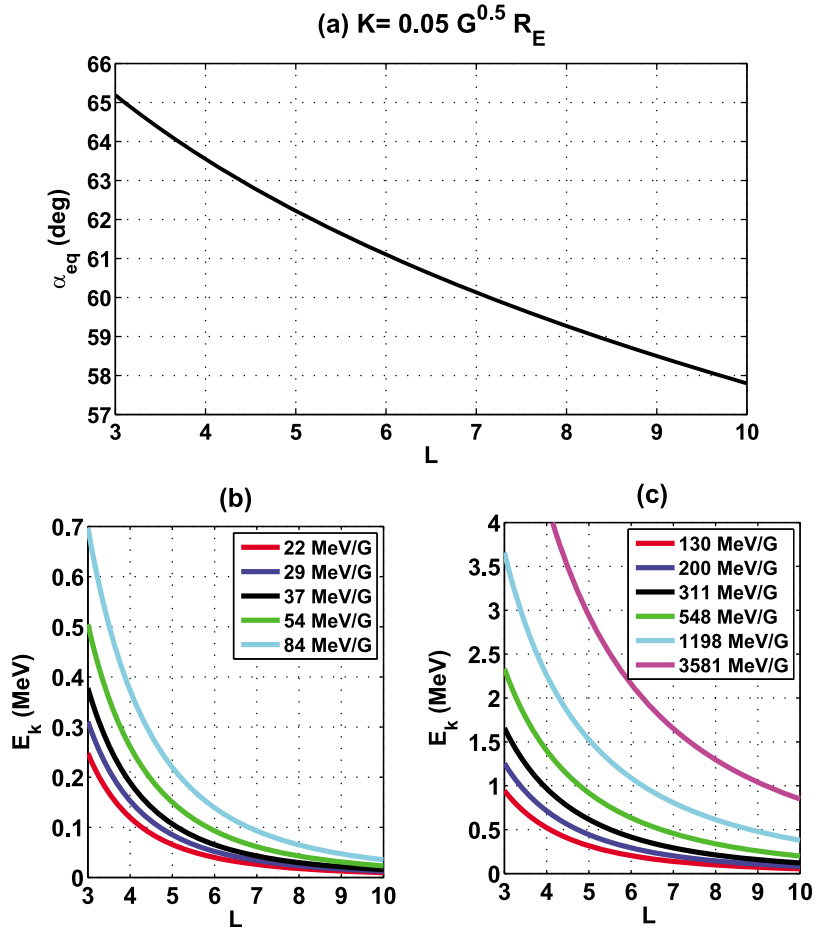

Figure 3. The dependences of equatorial pitch angle α_{eq} and electron energy E_k on L shell in dipole magnetic field model for the specified (μ, K) pairs.

spacecraft we calculate electron PSD for the (μ, K) pairs listed in Table 1. PSD conjunctions within $5.9 < L^* < 6.1$ are selected so that the corresponding electron energies are consistent with the THEMIS SST energy channels. Figure 5 shows the PSD conjunctions at the 11 specified μ values that correspond to the considered 11 SST energy channels for the four indicated THEMIS spacecraft pairs. The number of PSD conjunctions for each fixed PSC is given in Table 2. Because of the differences in satellite orbits and data availability, there are only several conjunction points for each energy channel between THEMISa and THEMISd (Figure 5a), insufficient for a reliable analysis. However, excellent agreement exists for all these PSD conjunctions. More conjunctions occur for the other satellite pairs, i.e., between THEMISb and THEMISc in Figure 5b, THEMISc and THEMISd in Figure 5c, and between THEMISd and THEMISe in Figure 5d. Despite a few outliers most of the PSD conjunctions for all the color-coded μ values are located at or very close to the diagonal lines, indicating good consistency between the electron flux observations from these individual THEMIS SST instruments. This consistency suggests that all THEMIS SST detectors respond similarly to the ambient electron radiation environment and that the difference in measured electron fluxes between the THEMIS SST and LANL SOPA instruments is likely due to systematic errors in the observations.

[15] With the selected 11 μ values (from 22 MeV/G to 3581 MeV/G) corresponding to the 11 THEMIS SST energy channels from 40 keV to 2159 keV for the fixed value of $K = 0.05\ G^{0.5}\ R_E$ at $L^* = 6$, cross-satellite calibrations of THEMIS (a–e) SST electron flux data are performed based on electron PSD conjunctions with the calibrated LANL-01A SOPA data for the considered 6 month period. The numbers of PSD conjunctions for each satellite pair are listed in Table 3. While the PSD conjunctions are quite few for the lowest value of μ = 22 MeV/G (or lowest-energy channel at 40 keV), there are considerable points for the other energy channels. Figures 6a–6f show the scatter of joint PSD points for the indicated six satellite pairs with respect to the color-coded μ value after intersatellite calibration. For each indicated satellite pair the dashed diagonal line of slope = 1 means perfect agreement. The electron PSD conjunctions between the LANL-01A and 1989–040 (GEO1989) satellites show excellent consistencies in magnitude as well as high-correlation coefficient (CC > 0.8) for all the 11 energy channels (Figures 6k and 6l), suggesting the reliability of LANL SOPA measurements as a standard for cross-instrument calibration. The calibrated electron PSD for the five THEMIS probes are presented in Figures 6a,

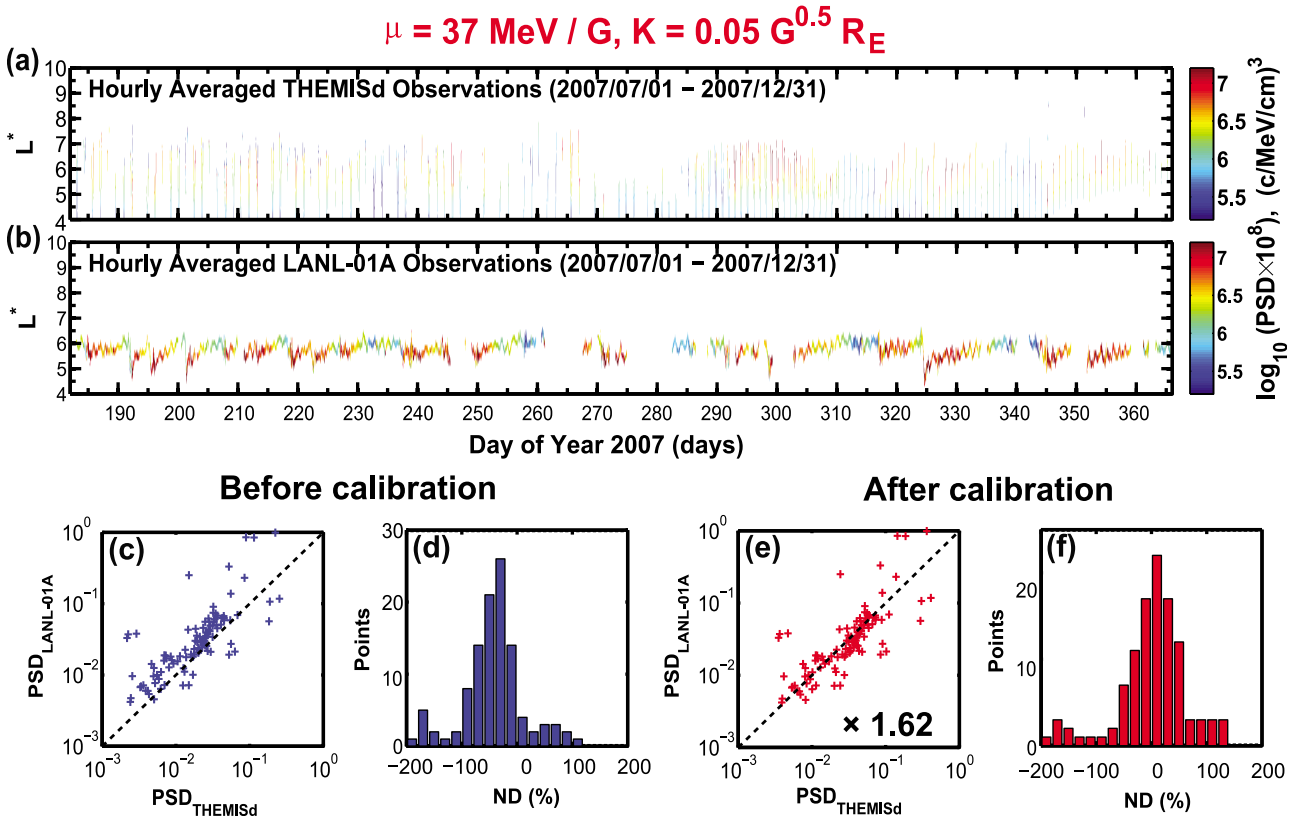

Figure 4. Hourly averaged electron PSD data inferred from (a) THEMISd SST and (b) LANL-01A SOPA data. (c) PSD conjunctions at 5.9 < L* < 6.1 for the satellite pair and (d) distribution of PSD conjunctions with normalized difference before calibration. The results after cross-satellite calibration are shown in Figures 4e and 4f. μ = 700 MeV G^{-1} and K = 0.11 $G^{0.5}$ R_E. Electron PSD is in units of c/MeV/cm^3, and the dashed diagonal of slope = 1 represents perfect cross-satellite calibration.

6c, 6e, 6g, and 6i, respectively. Most of the PSD conjunction occurrences after cross-satellite calibration lie at or very close to the diagonal, showing good agreements with the LANL-01A PSD data. The corresponding energy-dependent cross-correlation coefficients for each of the five satellite pairs (Figures 6b, 6d, 6f, 6h, and 6j) also indicate that there is good correlation between the THEMIS data and LANL-01A data, in particular for E_k < ~1 MeV.

[16] To quantify the systematic errors in the THEMIS SST data, Figure 6m shows the cross-satellite calibration factors for each THEMIS probe as a function of energy channel. To obtain these factors, for each energy channel we take the optimum constant that leads to the minimum values of averaged absolute difference and standard deviation of PSD conjunctions for the satellite pair under investigation. In general, the calibration factors (CF) for each THEMIS probe are similar: for E_k < ~200 keV CF > 1, indicating that the SST observations underestimate the electron fluxes at these lower-energy channels, while for E_k > 200 keV CF < 1, showing the overestimate of electron fluxes at these higher-energy channels of the THEMIS SST instrument. More specifically, compared to the LANL-01A SOPA data, the THEMIS SST measurements underestimate the electron fluxes within a factor of 2 for the 40–140 keV energy channels and overestimate the electron fluxes within a factor of 3 for the 204–2159 keV energy channel, as listed in Table 4. Figure 6n shows the normalized root mean square errors (NRMSE) between the LANL-01A and calibrated THEMIS PSD conjunctions as a function of energy channel, computed from

$$NRMSE(PSD_{LANL}, PSD_{THEMIS}) = \frac{\sqrt{\sum_{i=1}^{n} \left((PSD_{LANL})_i - (PSD_{THEMIS})_i\right)^2 / n}}{\sqrt{std(PSD_{LANL})} \cdot \sqrt{std(PSD_{THEMIS})}}, \quad (3)$$

where n is the number of PSD conjunctions for each energy channel and *std* means the standard deviation. Larger errors generally occur for the higher-energy channels of the THEMIS SST detector, as expected from the broader spreads of PSD conjunctions for larger μ values in the scatterplots and the relatively smaller correlation coefficients at higher energies. The evaluation of NRMSE can provide information about observation errors for each THEMIS SST instrument, which is useful for an optimal combination of observation data and physical model results through data assimilation technique [e.g., *Shprits et al.*, 2007; *Koller et al.*, 2007; *Ni et al.*, 2009a, 2009b].

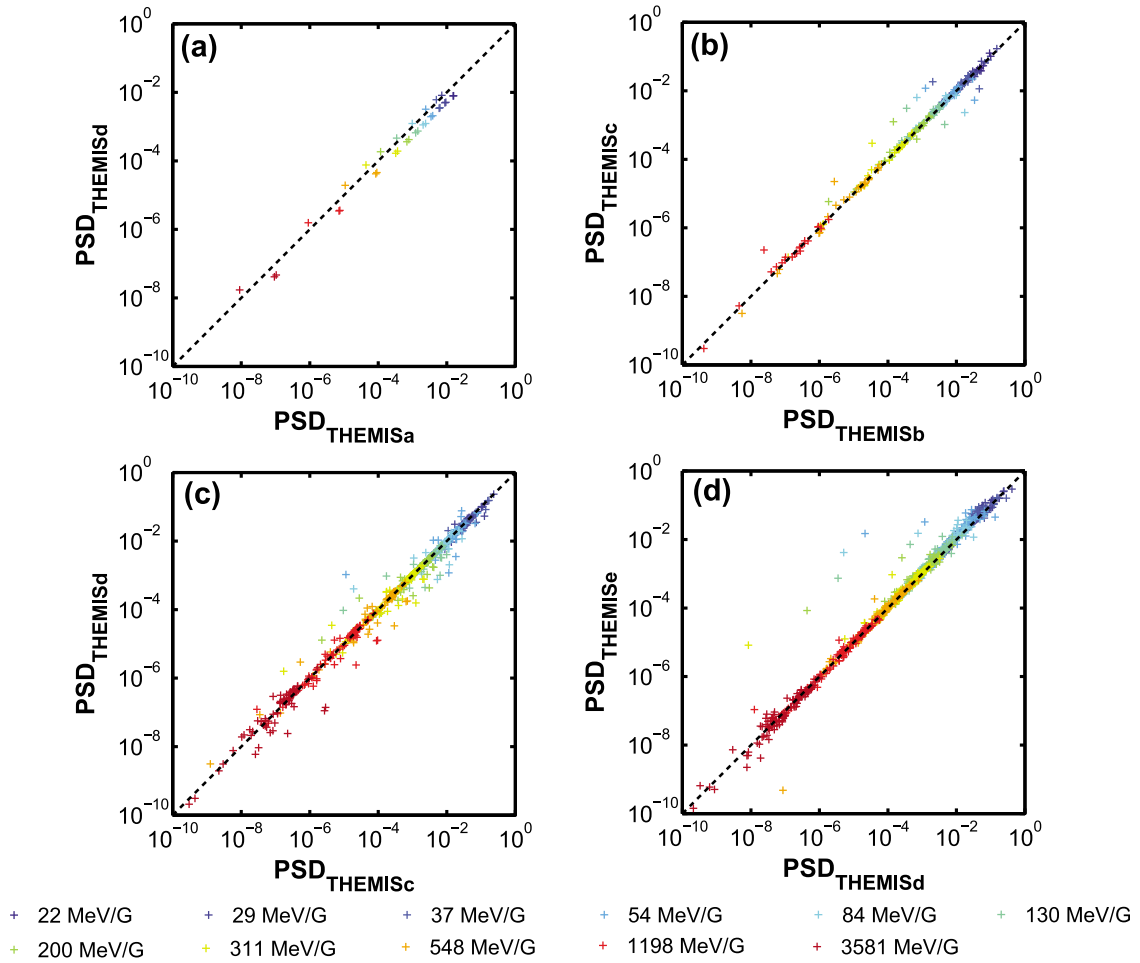

Figure 5. PSD conjunctions at $5.9 < L^* < 6.1$ corresponding to the color-coded μ values and a fixed value of $K = 0.05\ G^{0.5}\ R_E$ for the four THEMIS spacecraft pairs: (a) THEMISa and THEMISd, (b) THEMISb and THEMISc, (c) THEMISc and THEMISd, and (d) THEMISd and THEMISe. Electron PSD is in units of c/MeV/cm^3, and the dashed diagonal of slope = 1 represents perfect agreement.

[17] Incorporation of these energy channel dependent intersatellite calibration factors into the original THEMIS SST electron flux data can remove the systematic errors of the THEMIS SST measurements and establish an improved five-probe database of radiation belt electron fluxes. We use the T96 magnetic field model and the calibrated SST flux data to recalculate the electron PSD for each THEMIS spacecraft, which can be further used to study the radial gradient and temporal variation of electron PSD. We fix the value of the second adiabatic invariant $K = 0.025\ G^{0.5}\ R_E$, corresponding to electrons with $\alpha_{eq} = 69°$ at $L = 6$ in a dipole field model. We focus on a 2 day period starting from 20 July 2007 and including a pronounced sudden solar wind pressure enhancement. As shown in Figure 7e, a strong pressure pulse occurred around 9 UT on the first day with $\Delta P_{dyn} \geq 10$ nPa within 4 h. The compression of the magnetic field results in a considerable earthward movement of the magnetopause location (shown by the blue curve in Figure 7f) to $L_{MP} \approx 7$, based on the empirical model of *Shue et al.* [1997].

[18] Since the THEMIS satellites were close to the perigees when the magnetopause was compressed and moved to higher L shells when the magnetopause relaxed, the THEMIS probes were located in the magnetosphere during

Table 2. Number of Electron PSD Conjunctions Between the THEMIS Probes as a Function of the Selected 11 μ Values Corresponding to the 11 THEMIS SST Energy Channels With a Fixed Value of $K = 0.05\ G^{0.5}\ R_E$ and a Fixed L* Range of 5.9–6.1

	Number of PSD Conjunctions Between the THEMIS Probes										
μ (MeV/G)	22	29	37	54	84	130	200	311	548	1198	3581
THD versus THA	2	3	3	3	3	3	3	3	3	3	3
THC versus THB	0	17	23	27	27	27	27	27	27	27	26
THD versus THC	5	61	69	83	83	83	83	83	83	82	74
THE versus THD	7	90	118	118	118	118	118	118	118	118	104

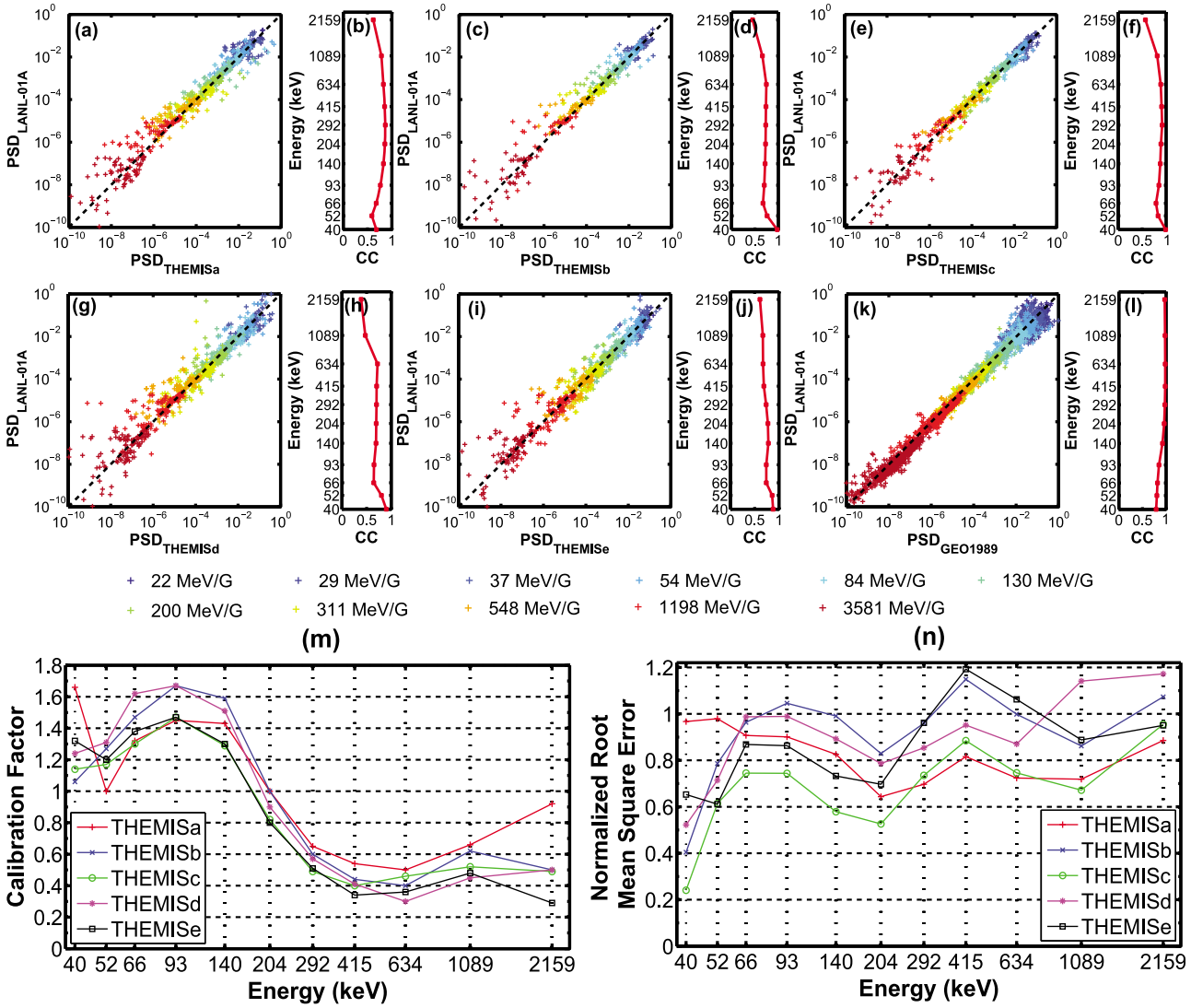

Figure 6. Cross-satellite calibration of THEMIS (a–e) SST data based on comparisons with LANL-01A data from 1 July to 31 December 2007. $K = 0.05\ G^{0.5}\ R_E$ and PSD conjunctions are obtained using T96 model and confined to $5.9 < L^* < 6.1$ for the color-coded μ values. PSD conjunctions after calibration are shown in Figures 6a, 6c, 6e, 6g, and 6i for THEMIS a–e with the correlation coefficients in Figures 6b, 6d, 6f, 6h, and 6j. PSD conjunctions and correlation coefficients between LANL-01A and GEO1989 are shown in Figures 6k and 6l. (m) Cross-satellite calibration factors and (n) normalized root mean square errors as a function of energy for each THEMIS probe. Electron PSD is in units of c/MeV/cm^3.

the interval of interest. The electron PSDs inferred from the measurements of THEMIS a–e, LANL-01A, and GEO1989 are shown in Figures 7a and 7b for μ = 700 MeV/G and 300 MeV/G, respectively. There are a number of features worthwhile to note: (1) While the THEMIS probes cover an L* range much broader than the LANL and GEO satellites, their PSD conjunctions at the same PSCs show quite good agreement in magnitude, suggestive of a reasonable cross-instrument calibration of the THEMIS SST flux observations. (2) The dropout in electron PSD on 20 July by at least 1 order of magnitude occurs together with the sudden enhancement of solar wind dynamic pressure and the Dst minimum of a small storm. The inward movement of the magnetopause owing to magnetospheric compression contributes to the losses of a large population of radiation belt electrons to the magnetopause. The resultant negative gradients in PSD further drive the outward radial diffusion of electrons at lower L shells [*Shprits et al.*, 2006]. The pronounced dropout occurs at both μ values corresponding to different electron energies, which is consistent with the energy-independent loss of electrons to the magnetopause following the outward radial diffusion; (3) after the pressure pulse, the electron PSD gradually builds up in the outer radiation belt on a timescale of several hours or ~1 day during the slow storm recovery phase. The relaxation of the magnetopause location allows more electrons move into the inner magnetosphere. Additionally, PSD peaks are also established within L* = 5–6, especially for the higher-energy electrons (~0.7–1 MeV) of μ = 700 MeV/G, suggesting a local acceleration process by chorus waves [e.g.,

Table 3. Number of Electron PSD Conjunctions for the Indicated Six Satellite Pairs as a Function of the Selected 11 μ Values Corresponding to the 11 THEMIS SST Energy Channels With a Fixed Value of K = 0.025 $G^{0.5}$ R_E and a Fixed L* Range of 5.9–6.1

	Number of PSD Conjunctions for the Six Satellite Pairs										
μ (MeV/G)	22	29	37	54	84	130	200	311	548	1198	3581
LANL versus THA	8	59	80	85	85	85	85	86	86	86	78
LANL versus THB	4	46	53	54	54	54	54	54	54	54	54
LANL versus THC	4	48	59	61	61	61	61	61	61	61	59
LANL versus THD	5	80	109	122	125	125	125	125	125	125	119
LANL versus THE	12	86	109	115	117	117	117	117	117	117	110
LANL versus GEO	668	948	951	956	957	957	958	961	960	960	940

Meredith et al., 2003; *Horne et al.*, 2005; *Thorne et al.*, 2005; *Summers et al.*, 2007; *Shprits et al.*, 2007, 2008b; *Xiao et al.*, 2009]. Overall, Figure 7 shows a clear correlation between electron PSD dropouts and the solar wind pressure pulse, which can be attributed to the combination of losses to the magnetopause and outward radial diffusion. The gradual buildup of electron PSD after the abrupt pressure enhancement likely results from a combination of local acceleration and inward and outward radial diffusion that refills the main phase PSD dropout during the outward movement of the magnetopause [*Subbotin et al.*, 2010; *Xiao et al.*, 2010].

4. Discussion

[19] While the correlation coefficients above 350 keV are smaller than at lower energies, such a high correlation of >0.7–0.8 is nonetheless surprising. The high-energy channels on the "F" detector are affected significantly by the ion fluxes. Since an energetic electron cannot deposit much direct energy on "F," what is measured by the detector is, in part, electron recoils in the lattice, or penetrating electrons, or gamma rays from the electron deposition in the "T" detector or the walls. This may potentially explain the "overestimation" of the fluxes at these energies. Part of the surprise is due to the expectation that in the heart of the proton belt the high-energy channels on the "T" detector will be responding to proton fluxes and detector count rates will not correlate with energetic electron fluxes. Nevertheless, a good agreement between the THEMIS SST and LANL-01A SOPA electron PSD measurements is observed after the cross-satellite calibration, suggesting that much of the systematic error associated with the SST instrument has been empirically removed.

[20] To compute electron PSD using the omnidirectional fluxes from the LANL-01A SOPA measurements, radiation belt electron differential flux distribution has been assumed to follow a power law function of the sine of pitch angle and an exponentially decreasing energy spectrum. However, there are a number of studies showing that highly energetic electrons can be better modeled by relativistic kappa-type distributions [e.g., *Xiao*, 2006; *Xiao et al.*, 2008a], which are found to fit well with the solar energetic particles [*Xiao et al.*, 2008b] and the observations at the geostationary orbit [*Xiao et al.*, 2008c]. It is apparent that using a more complex and probably more reasonable electron distribution such as a relativistic kappa-type distribution can alter the modeled differential flux at the energy and pitch angle specified for fixed adiabatic invariants and therefore modify the inferred electron PSD versus L* distribution. As a consequence, the relative differences between PSD conjunctions may vary, thereby affecting the evaluation of intercalibration factor. Examining the effects of adopting such relativistic kappa-type distributions on our presented results is outside the scope of this study but is worth a detailed investigation to be demonstrated in our further studies.

[21] In the present study, we have restricted PSD conjunctions to a narrow range $5.9 < L^* < 6.1$ to ensure that the PSD conjunctions for each of the selected μ values correspond well to each of the considered energy channels. The limitation of this treatment is that we exclude useful conjunctions at other L* values and thus have a smaller number of PSD conjunctions, particularly for the lowest-energy channel we considered (40 keV, Table 3). We note that through evaluation of electron energies associated with PSD conjunctions at all L* values, a larger database of PSD conjunctions can be established for each energy channel, which will be a follow-up study to further improve and validate our intersatellite calibration methodology. In the present study, we have dealt with the THEMIS SST data obtained using the r6931 (released 12 November 2009) version of

Table 4. Cross-Instrument Calibration Factors for all the Five THEMIS SST Electron Flux Measurements as a Function of Energy Channel Based on PSD Conjunctions With the LANL-01A SOPA Data

	Intercalibration Factors										
E_k (keV)	40	52	66	93	140	204	292	415	634	1089	2159
THA	1.66	1.0	1.32	1.45	1.43	1.0	0.65	0.54	0.5	0.66	0.92
THB	1.06	1.27	1.47	1.67	1.59	1.0	0.6	0.44	0.4	0.62	0.5
THC	1.14	1.17	1.3	1.47	1.29	0.82	0.49	0.4	0.46	0.52	0.49
THD	1.24	1.31	1.62	1.67	1.51	0.9	0.57	0.41	0.3	0.45	0.5
THE	1.32	1.2	1.38	1.47	1.3	0.8	0.51	0.34	0.36	0.48	0.29

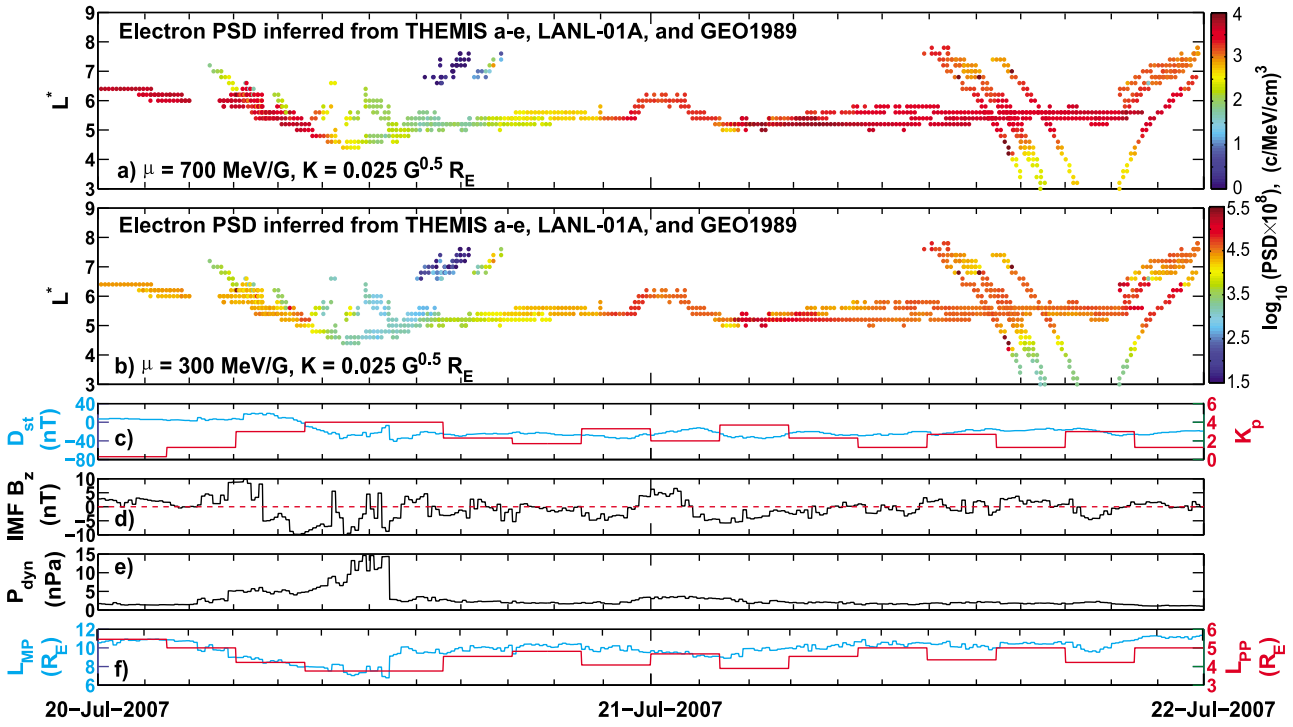

Figure 7. Ten minute averaged PSDs inferred using the T96 model for (a) K = 0.025 $G^{0.5}$ R_E and μ = 700 MeV/G and for (b) K = 0.025 $G^{0.5}$ R_E and μ = 300 MeV/G for THEMIS a–e, LANL-01A, and GEO1989 during a pressure pulse event. (b) Reanalysis results using all seven satellite data sets. (c) Dst, (d) IMF Bz, (e) solar wind dynamic pressure, and (f) the locations of magnetopause (blue curve) and plasmapause (red curve).

the THEMIS software. Since there will be continued calibration to the THEMIS SST data by the THEMIS team, we will track the changes in THEMIS software and provide the updates to the cross-satellite calibration factors via our website (http://yssvnl.atmos.ucla.edu/projects/THEMIS/intercalibration).

[22] Good consistency in electron PSD conjunctions between the five THEMIS probes (Figure 5) indicates that the SST instrument aboard each spacecraft responds in a similar way to the ambient radiation environment, which is also evident from the similarity of cross-satellite calibration factors (Figure 6m) for each THEMIS satellite. The obtained cross-satellite calibration factors show a strong dependence on energy channel. For E_k < ~200 keV our results indicate that the THEMIS SST observations underestimate the electron fluxes, consistent with the unrealistic substantial flux drops at the lowest SST energy channels compared to the fluxes of the highest THEMIS ESA energy channels (data available at http://www.virbo.org/Image:THEMIS-SST.ppt). Although the convection electric field directed from dawn to dusk [*Volland*, 1978] may alter the energies of 10′s keV–~100 keV electrons, both the high-value correlation coefficients and the consistency in PSD conjunctions after cross-satellite calibration (Figures 6a–6j) for the associated SST energy channels imply that the dawn-to-dusk convection electric field has a relatively minor influence on the transport of these 10′s keV–~100 keV electrons for the relatively quiet period considered. After the cross-satellite calibration the proximity of PSD conjunctions to the diagonal lines of slope = 1 is evident up to $E_k \approx 1$ MeV. The relatively broad spread of the PSD conjunctions at ~2 MeV is in line with the lowest correlation between the SST and SOPA flux measurements for this energy channel. Detailed analysis of the T channels may provide more direct and more accurate derivation of ambient energetic electron fluxes and will be a subject of future research. T channel measurements will be also tested and cross-satellite calibrated using the methodology developed in this study.

[23] The cross-satellite calibrated THEMIS SST flux measurements, in combination with the LANL and GEO SOPA observations at geosynchronous orbit, provide good data coverage in both space and time to evaluate the temporal variations and the radial gradients of electron PSD. During a case study of a 2 day period that included a pronounced solar wind pressure pulse event and a small storm with minimum Dst = −40 nT, we captured a clear correlation between electron PSD dropouts and the solar wind pressure pulse. This result is consistent with *Shprits et al.* [2006], *Turner and Li* [2008], *Ohtani et al.* [2009], and *Turner et al.* [2010]. They studied the dynamics of radiation belt electrons at and beyond geostationary orbit in association with disturbed solar wind conditions, finding that solar wind and geomagnetic conditions are important to the variability of radiation belt electron PSD and that magnetopause shadowing can be a plausible loss process for geosynchronous MeV electrons. While the formation of PSD dropouts associated with the pressure pulse is most likely attributed to

the combination of magnetopause shadowing and outward radial diffusion, *Usanova et al.* [2008] also proposed that magnetospheric compression-related EMIC Pc1 waves may also play a role in driving efficient loss of radiation belt relativistic electrons.

[24] Recently, instead of estimating the PSD gradient by analyzing the inferred PSD versus L* distributions which are generally sparse, a number of studies [*Shprits et al.*, 2007; *Koller et al.*, 2007; *Ni et al.*, 2009a, 2009b] have assimilated electron PSD data from single or multiple satellites with a radial diffusion model [*Shprits et al.*, 2006, 2008a] in an optimal way to establish the radial profile of radiation belt electron PSD with high resolution in space and time for radiation belt studies. Reconstruction of such a long-term global picture of radiation belt electron PSD based on multiple-satellite measurements, including the cross-satellite calibrated five-probe THEMIS database, can provide detailed information about the magnitude, spatial extent, and temporal evolution of dropouts and peaks in electron PSD. Such information can be further used to better understand the underlying physical mechanisms responsible for the dynamic responses of radiation belt electrons to solar activity, which will be a subject of follow-up studies.

[25] It is anticipated that the intersatellite calibration method and the analysis tool of the THEMIS SST measurements presented in this study will be optimized for analysis, calibration, and assimilation of measurements from the upcoming RBSP mission [*Kintner and Living With a Star Geospace Mission Definition Team*, 2002] and possibly other missions such as ERG [*Shiokawa et al.*, 2006], ORBITALS [*Mann et al.*, 2006], RESONANCE [*Zelenyi et al.*, 2004], and LOMONOSOV (http://www.russianspaceweb.com/2011.html) with high resolution in space, energy, pitch angle, and time.

5. Concluding Remarks

[26] By confining the PSD occurrences of trapped radiation belt electrons to $5.9 < L^* < 6.1$ and selecting 11 μ values from 22 MeV/G to 3581 MeV/G, we have performed an energy-dependent cross-satellite calibration of the THEMIS SST flux measurements at 11 energy channels from 40 keV to 2159 keV based on PSD conjunctions at fixed PSCs with LANL-01A SOPA observations for a half year period starting from 1 July 2007. The cross-satellite calibrated THEMIS SST data, together with the LANL-01A and GEO1989 SOPA data, were then used for a case study of the temporal variation and radial gradient of radiation belt electron PSD during a pronounced solar wind pressure pulse event. The present study and the main conclusions can be summarized as follows:

[27] (1) Consistency in PSD conjunctions between the five THEMIS probes indicates that the SST instrument aboard each spacecraft responds quite similarly to the ambient electron radiation environment. Comparisons of electron PSDs between the THEMIS SST and LANL SOPA measurements and calculations of the correlation coefficients show that that the differences in electron fluxes are likely due to systematic errors in the THEMIS SST fluxes.

[28] (2) Compared to the LANL-01A SOPA data, the THEMIS SST data underestimate the electron fluxes within a factor of 2 for the 40–140 keV energy channels and overestimate the electron fluxes within a factor of 3 for the 204–2159 keV energy channels. The energy-dependent intersatellite calibration factors for each THEMIS probe are similar. After cross-satellite calibration most of the THEMIS-LANL PSD conjunctions show good agreement with each other, particular for the SST energy channels $E_k \leq 1$ MeV.

[29] (3) A case study of the variation of electron PSD during a pronounced solar wind pressure pulse event using the calibrated THEMIS SST data and the LANL and GEO SOPA observations demonstrates a clear correlation between electron PSD dropouts and the solar wind pressure pulse, owing to a combination of magnetopause shadowing and outward radial diffusion. The gradual buildup of electron PSD after the pressure relaxation is probably attributed to a combination effect of local acceleration and inward and outward radial diffusion that can refill the main phase PSD dropout during the outward movement of the magnetopause.

[30] It is clear that incorporation of reliable, energy channel dependent cross-satellite calibration factors into the original THEMIS SST electron flux data can remove the systematic errors of the THEMIS SST measurements and establish an improved five-probe THEMIS database of radiation belt electron fluxes. While we have proposed preliminary explanations for the response of radiation belt electron PSD to a sudden solar wind pressure enhancement, the response of the radiation belt electron PSD to various drivers still needs to be treated in a quantitative and systematic way through a long-term analysis of the radial profile of electron PSD, based on multiple satellite measurements including calibrated THEMIS SST data.

[31] **Acknowledgments.** We thank Amanda Leung for help with the calculations of L* and the developers of the ONERA-DESP library, including D. Boscher, S. Bourdarie, P. O'Brien, and T. Guild. We also thank Reiner Friedel for providing the LANL SOPA data and Yue Chen for helpful discussion. This work was supported by the Lab Research Fee grant 09-LR-04-116720-SHPY.

[32] Masaki Fujimoto thanks the reviewers for their assistance in evaluating this paper.

References

Agostinelli, S., et al. (2003), Geant4: A simulation toolkit, *Nucl. Instrum. Methods Phys. Res., Sect. A*, *506*, 250–303, doi:10.1016/S0168-9002(03)01368-8.

Angelopoulos, V. (2008), The THEMIS mission, *Space Sci. Rev.*, *141*, 5–34, doi:10.1007/s11214-008-9336-1.

Angelopoulos, V., et al. (2008), First results from the THEMIS mission, *Space Sci. Rev.*, *141*, 453–476, doi:10.1007/s11214-008-9378-4.

Auster, U., et al. (2008), The THEMIS fluxgate magnetometer, *Space Sci. Rev.*, *141*, 235–264, doi:10.1007/s11214-008-9365-9.

Belian, R., G. Gisler, T. Cayton, and R. Christensen (1992), High-Z energetic particles at geosynchronous orbit during the great solar proton event series of October 1989, *J. Geophys. Res.*, *97*(A11), 16,897–16,906, doi:10.1029/92JA01139.

Bonnell, J. W., et al. (2008), The electric field instrument (EFI) for THEMIS, *Space Sci. Rev.*, *141*, 303–341, doi:10.1007/s11214-008-9469-2.

Chen, Y., R. H. W. Friedel, G. D. Reeves, T. G. Onsager, and M. F. Thomsen (2005), Multisatellite determination of the relativistic electron phase space density at geosynchronous orbit: Methodology and results during geomagnetically quiet times, *J. Geophys. Res.*, *110*, A10210, doi:10.1029/2004JA010895.

Cully, C. M., R. E. Ergun, K. Stevens, A. Nammari, and J. Westfall (2008), The THEMIS digital fields board, *Space Sci. Rev.*, *141*, 343–355, doi:10.1007/s11214-008-9417-1.

Friedel, R. H. W., S. Bourdarie, and T. E. Cayton (2005), Intercalibration of magnetospheric energetic electron data, *Space Weather*, *3*, S09B04, doi:10.1029/2005SW000153.

Gannon, J. L., X. Li, and D. Heynderickx (2007), Pitch angle distribution analysis of radiation belt electrons based on Combined Release and Radiation Effects Satellite Medium Electrons A data, *J. Geophys. Res.*, *112*, A05212, doi:10.1029/2005JA011565.

Gu, X., Z. Zhao, B. Ni, Y. Shprits, and C. Zhou (2011), Statistical analysis of pitch angle distribution of radiation belt energetic electrons near the geostationary orbit: CRRES observations, *J. Geophys. Res.*, *116*, A01208, doi:10.1029/2010JA016052.

Horne, R. B., R. M. Thorne, S. A. Glauert, J. M. Albert, N. P. Meredith, and R. R. Anderson (2005), Timescale for radiation belt electron acceleration by whistler mode chorus waves, *J. Geophys. Res.*, *110*, A03225, doi:10.1029/2004JA010811.

Kintner, P. M., and the Living With a Star Geospace Mission Definition Team (2002), The LWS geospace storm investigations: Exploring the extremes of space weather, *Tech. Memo., TM-2002-211613*, NASA, Hanover, Md.

Koller, J., Y. Chen, G. D. Reeves, R. H. W. Friedel, T. E. Cayton, and J. A. Vrugt (2007), Identifying the radiation belt source region by data assimilation, *J. Geophys. Res.*, *112*, A06244, doi:10.1029/2006JA012196.

Le Contel, O., et al. (2008), First results of the THEMIS searchcoil magnetometers, *Space Sci. Rev.*, *141*, 509–534, doi:10.1007/s11214-008-9371-y.

Li, W., R. M. Thorne, V. Angelopoulos, J. Bortnik, C. M. Cully, B. Ni, O. LeContel, A. Roux, U. Auster, and W. Magnes (2009a), Global distribution of whistler-mode chorus waves observed on the THEMIS spacecraft, *Geophys. Res. Lett.*, *36*, L09104, doi:10.1029/2009GL037595.

Li, W., R. M. Thorne, V. Angelopoulos, J. W. Bonnell, J. P. McFadden, C. W. Carlson, O. LeContel, A. Roux, K. H. Glassmeier, and H. U. Auster (2009b), Evaluation of whistler-mode chorus intensification on the nightside during an injection event observed on the THEMIS spacecraft, *J. Geophys. Res.*, *114*, A00C14, doi:10.1029/2008JA013554.

Li, W., et al. (2010), THEMIS analysis of observed equatorial electron distributions responsible for the chorus excitation, *J. Geophys. Res.*, *115*, A00F11, doi:10.1029/2009JA014845.

Mann, I. R., et al. (2006), The Outer Radiation Belt Injection, Transport, Acceleration and Loss Satellite (ORBITALS): A Canadian small satellite mission for ILWS, *Adv. Space Res.*, *38*, 1838–1860, doi:10.1016/j.asr.2005.11.009.

McFadden, J. P., C. W. Carlson, D. Larson, V. Angelopoulos, M. Ludlam, R. Abiad, B. Elliott, P. Turin, and M. Marckwordt (2008), The THEMIS ESA plasma instrument and in-flight calibration, *Space Sci. Rev.*, *141*, 277–302, doi:10.1007/s11214-008-9440-2.

Meredith, N. P., M. Cain, R. B. Horne, R. M. Thorne, D. Summers, and R. R. Anderson (2003), Evidence for chorus-driven electron acceleration to relativistic energies from a survey of geomagnetically disturbed periods, *J. Geophys. Res.*, *108*(A6), 1248, doi:10.1029/2002JA009764.

Ni, B., R. M. Thorne, Y. Y. Shprits, and J. Bortnik (2008), Resonant scattering of plasma sheet electrons by whistler-mode chorus: Contribution to diffuse auroral precipitation, *Geophys. Res. Lett.*, *35*, L11106, doi:10.1029/2008GL034032.

Ni, B., Y. Shprits, T. Nagai, R. Thorne, Y. Chen, D. Kondrashov, and H.-J. Kim (2009a), Reanalyses of the radiation belt electron phase space density using nearly equatorial CRRES and polar-orbiting Akebono satellite observations, *J. Geophys. Res.*, *114*, A05208, doi:10.1029/2008JA013933.

Ni, B., Y. Shprits, R. Thorne, R. Friedel, and T. Nagai (2009b), Reanalysis of relativistic radiation belt electron phase space density using multisatellite observations: Sensitivity to empirical magnetic field models, *J. Geophys. Res.*, *114*, A12208, doi:10.1029/2009JA014438.

Ohtani, S., Y. Miyoshi, H. J. Singer, and J. M. Weygand (2009), On the loss of relativistic electrons at geosynchronous altitude: Its dependence on magnetic configurations and external conditions, *J. Geophys. Res.*, *114*, A01202, doi:10.1029/2008JA013391.

Olson, W. P., and K. A. Pfitzer (1977), Magnetospheric magnetic field modeling, *Annu. Sci. Rep. F44620-75-C-0033*, Air Force Off. of Sci. Res, Arlington, Va.

Reeves, G. D., K. L. McAdams, R. H. W. Friedel, and T. P. O'Brien (2003), Acceleration and loss of relativistic electrons during geomagnetic storms, *Geophys. Res. Lett.*, *30*(10), 1529, doi:10.1029/2002GL016513.

Roux, A., O. LeContel, C. Coillot, A. Bouabdellah, B. de la Porte, D. Alison, S. Ruocco, and M. C. Vassal (2008), The search coil magnetometer for THEMIS, *Space Sci. Rev.*, *141*, 265–275, doi:10.1007/s11214-008-9455-8.

Selesnick, R. S., and S. G. Kanekal (2009), Variability of the total radiation belt electron content, *J. Geophys. Res.*, *114*, A02203, doi:10.1029/2008JA013432.

Shiokawa, K., et al. (2006), ERG–A small-satellite mission to investigate the dynamics of the inner magnetosphere, *Adv. Space Res.*, *38*, 1861–1869, doi:10.1016/j.asr.2005.05.089.

Shprits, Y., D. Kondrashov, Y. Chen, R. Thorne, M. Ghil, R. Friedel, and G. Reeves (2007), Reanalysis of relativistic radiation belt electron fluxes using CRRES satellite data, a radial diffusion model, and a Kalman filter, *J. Geophys. Res.*, *112*, A12216, doi:10.1029/2007JA012579.

Shprits, Y. Y., R. M. Thorne, R. Friedel, G. D. Reeves, J. Fennell, D. N. Baker, and S. G. Kanekal (2006), Outward radial diffusion driven by losses at magnetopause, *J. Geophys. Res.*, *111*, A11214, doi:10.1029/2006JA011657.

Shprits, Y. Y., S. R. Elkington, N. P. Meredith, and D. A. Subbotin (2008a), Review of modeling of losses and sources of relativistic electrons in the outer radiation belts: I. Radial transport, *J. Atmos. Sol. Terr. Phys.*, *70*, 1679–1693, doi:10.1016/j.jastp.2008.06.008.

Shprits, Y. Y., D. A. Subbotin, N. P. Meredith, and S. R. Elkington (2008b), Review of modeling of losses and sources of relativistic electrons in the outer radiation belts: II. Local acceleration and loss, *J. Atmos. Sol. Terr. Phys.*, *70*, 1694–1713, doi:10.1016/j.jastp.2008.06.014.

Shue, J.-H., J. K. Chao, H. C. Fu, C. T. Russell, P. Song, K. K. Khurana, and H. J. Singer (1997), A new functional form to study the solar wind control of the magnetopause size and shape, *J. Geophys. Res.*, *102*(A5), 9497–9511, doi:10.1029/97JA00196.

Sibeck, D. G., and V. Angelopoulos (2008), THEMIS science objectives and mission phases, *Space Sci. Rev.*, *141*, 35–59, doi:10.1007/s11214-008-9393-5.

Subbotin, D., Y. Shprits, and B. Ni (2010), Three-dimensional VERB radiation belt simulations including mixed diffusion, *J. Geophys. Res.*, *115*, A03205, doi:10.1029/2009JA015070.

Summers, D., B. Ni, and N. P. Meredith (2007), Timescales for radiation belt electron acceleration and loss due to resonant wave-particle interactions: 2. Evaluation for VLF chorus, ELF hiss, and electromagnetic ion cyclotron waves, *J. Geophys. Res.*, *112*, A04207, doi:10.1029/2006JA011993.

Thorne, R. M., R. B. Horne, S. A. Glauert, N. P. Meredith, Y. Shprits, D. Summers, and R. R. Anderson (2005), The influence of wave-particle interactions on relativistic electron dynamics during storms, in *Inner Magnetosphere Interactions: New perspectives From Imaging*, *Geophys. Monogr. Ser*, vol. 159, edited by J. Burch, M. Schulz, and H. Spence, 101 pp., AGU, Washington, D. C.

Tsyganenko, N. A., and D. P. Stern (1996), Modeling the global magnetic field of the large-scale Birkeland current systems, *J. Geophys. Res.*, *101*(A12), 27,187–27,198, doi:10.1029/96JA02735.

Turner, D. L., and X. Li (2008), Radial gradients of phase space density of the outer radiation belt electrons prior to sudden solar wind pressure enhancements, *Geophys. Res. Lett.*, *35*, L18101, doi:10.1029/2008GL034866.

Turner, D. L., X. Li, G. D. Reeves, and H. J. Singer (2010), On phase space density radial gradients of Earth's outer-belt electrons prior to sudden solar wind pressure enhancements: Results from distinctive events and a superposed epoch analysis, *J. Geophys. Res.*, *115*, A01205, doi:10.1029/2009JA014423.

Usanova, M. E., I. R. Mann, I. J. Rae, Z. C. Kale, V. Angelopoulos, J. W. Bonnell, K.-H. Glassmeier, H. U. Auster, and H. J. Singer (2008), Multipoint observations of magnetospheric compression-related EMIC Pc1 waves by THEMIS and CARISMA, *Geophys. Res. Lett.*, *35*, L17S25, doi:10.1029/2008GL034458.

Vampola, A. L. (1998), Outer zone energetic electron environment update, in *Conference on the High Energy Radiation Background in Space*, pp. 128–136, IEEE Press, Piscataway, N. J.

Volland, H. (1978), A model of the magnetospheric electric convection field, *J. Geophys. Res.*, *83*(A6), 2695–2699, doi:10.1029/JA083iA06p02695.

Xiao, F. (2006), Modelling energetic particles by a relativistic kappa-loss-cone distribution function in plasmas, *Plasma Phys. Controlled Fusion*, *48*, 203–213, doi:10.1088/0741-3335/48/2/003.

Xiao, F., L. Chen, and J. Li (2008a), Energetic particles modeled by a generalized relativistic kappa-type distribution function in plasmas, *Plasma Phys. Controlled Fusion*, *50*, 105002, doi:10.1088/0741-3335/50/10/105002.

Xiao, F., Q. Zhou, C. Li, and A. Cai (2008b), Modeling solar energetic particle by a relativistic kappa-type distribution, *Plasma Phys. Controlled Fusion*, *50*, 062001, doi:10.1088/0741-3335/50/6/062001.

Xiao, F., C. Shen, Y. Wang, H. Zheng, and S. Wang (2008c), Energetic electron distributions fitted with a relativistic kappa-type function at geosynchronous orbit, *J. Geophys. Res.*, *113*, A05203, doi:10.1029/2007JA012903.

Xiao, F., Z. Su, H. Zheng, and S. Wang (2009), Modeling of outer radiation belt electrons by multidimensional diffusion process, *J. Geophys. Res.*, *114*, A03201, doi:10.1029/2008JA013580.

Xiao, F., Z. Su, H. Zheng, and S. Wang (2010), Three-dimensional simulations of outer radiation belt electron dynamics including cross-diffusion terms, *J. Geophys. Res.*, *115*, A05216, doi:10.1029/2009JA014541.

Zelenyi, L. M., et al. (2004), Russian space program: Experiments in solar-terrestrial physics, *Proc. Intl. Astron. Union*, 573–580, doi:10.1017/S1743921304006921.

V. Angelopoulos, Institute of Geophysics and Planetary Physics, University of California, Los Angeles, CA 90095, USA.

X. Gu, Department of Space Physics, Wuhan University, #129 Luoyue Rd., Wuhan, Hubei 430079, China.

M. Hartinger, Department of Earth and Space Sciences, University of California, 595 Charles Young Dr., Box 951567, Los Angeles, CA 90095, USA.

D. Larson, Space Sciences Laboratory, University of California, 7 Gauss Way, Berkeley, CA 94720, USA.

B. Ni and Y. Shprits, Department of Atmospheric and Oceanic Sciences, University of California, 405 Hilgard Ave., Box 951565, Los Angeles, CA 90095, USA. (bbni@atmos.ucla.edu)